PAPER

Electrochemical and electrical performances of cobalt chloride (CoCl$_2$) doped polyaniline (PANI)/graphene nanoplate (GNP) composite†

Sandip Maiti and B. B. Khatua*

The present study represents a simple and scalable method that involves *in situ* polymerization of cobalt chloride (CoCl$_2$·6H$_2$O) doped aniline in the presence of graphene nanoplates (GNPs) in HCl medium, for the preparation of CoCl$_2$ doped polyaniline (PANI)/GNP composites (PGC) as a supercapacitor electrode material with noteworthy performance. The maximum specific capacitance and energy density of the PGC composites were found to be $\approx$634 F g^{-1} and $\approx$427 W h kg^{-1}, respectively, at a 10 mV s^{-1} scan rate. Through judicious control of the GNP content and CoCl$_2$ doped PANI in the composites, a very high electrical conductivity ($\approx$12.2 S cm^{-1}) was achieved at unprecedented low GNP content. The PGC composites also exhibited high alternating current (AC) electrical conductivity in the frequency region of $\sim$10^1 to $\sim$10^7 Hz. The morphology of the composites was successfully studied by field emission scanning electron microscopy (FESEM) and high resolution transmission electron microscopy (HRTEM).

1. Introduction

In recent times, the popularity of different portable electronic devices and motor vehicles has increased the requirement of energy storage devices. In this regard, high performance capacitors and different batteries (Li-ion, Pb-acetate *etc.*) are of major interest in different scientific research areas. Supercapacitors are also known as electrochemical capacitors or ultracapacitors which are a great source of a huge amount of energy in a very short period of time and are crucial for surge power delivery. Due to their high power density, rapid charging–discharging rates and long cycle life (>100 000 cycles), supercapacitors have attracted great attention in various electronic and device applications.[1–3] Supercapacitors are generally used as complementary devices to fuel cells and batteries, which have high energy densities but are unable to supply a high power on a short time scale. Electrochemical capacitors have been considered as promising high-power sources for digital communication devices and electric vehicles.[4] Supercapacitors have been considered as critical components for the next generation all electric cars and cars based on fuel cells like the direct methanol fuel cell (DMFC), and the hydrogen fuel cell.[5,6] Supercapacitors are classified into two categories depending on the charge-storage mechanism:[7–10] (a) electrical double-layer capacitors (EDLCs) in which

the capacitance arises from the charge separation at the electrode–electrolyte interface. The charge storage mechanism is of non-faradaic type. EDLCs, using carbon-based active materials with high surface areas, build up electrical charge at the electrode–electrolyte interface. Usually, EDLCs have high power density but suffer from low capacitance and low rate capability. Secondly, (b) pseudocapacitors utilizing fast and reversible surface or near surface reactions for charge storage. Electrode materials for pseudocapacitors with certain metal oxides (MnO$_2$, RuO$_2$ *etc.*) or conducting polymers as electrode materials arise from faradaic reactions occurring at the electrode–electrolyte interface. Compared with EDLC-based capacitors, pseudocapacitors based on transition metal oxides, nitrides, and conducting polymers could provide higher specific capacitance but suffer from disadvantages such as higher cost and low conductivity. Therefore, there is currently an impending need to improve their performance to meet the increasing urgent demand for energy storage and stringent requirements in a variety of potential applications. The charge storage mechanism in pseudocapacitive materials gives us clues and directs strategies in the realization of high-performance supercapacitors. Achieving high power and energy densities, high specific surface area, high electronic conductivity, and fast cation intercalation/de-intercalation processes is very important. While the storage mechanism in carbon-based EDLCs occurs through electrostatic forces, fast faradaic redox reactions are responsible for the charge storage mechanism in pseudocapacitors.

Transition metal oxides have been explored as potential electrode materials for use in supercapacitors; their charge

Materials Science Centre, Indian Institute of Technology, Kharagpur-721302, India. E-mail: khatuabb@matsc.iitkgp.ernet.in; Fax: +91 3222 255303; Tel: +91 3222 283982

storage mechanisms are based predominantly on pseudoca-pacitance.[11,12] RuO_2 has been found to have high capacitance due to its advantageous redox transitions, however, the high cost of Ru is the major concern for commercial acceptance. The present trend in the ongoing research on supercapacitors is to develop economical electrode materials with a high capacity for charge storage and energy density. Cheap metal oxides with comparable characteristics, for example, oxides of Ni, Co, In, Sn, Fe, Mn, and so forth are being investigated and conducting polymers are another class of material under investigation due to their excellent electrochemical properties and low cost. Among the various conducting polymers such as polyaniline (PANI), polypyrrole (PPY), polythiophene (PTH) and their derivatives, polyaniline (PANI) has been studied extensively because of its cost-effective and easy synthesis procedure, good environmental stability, redox reversibility, and high electrical conductivity.[13] However, chemically pre-pared nanostructured conducting polymers are usually pow-dery and insulating in their doping states. Carbon-based nanomaterials having a high surface area and good electrical conductivity have been attracting the attention of the scientific community for different applications.[14] These carbon based nanomaterials (activated carbon, carbon nanotubes, and graphene) have been used as substrates for metal oxide nanoparticles for supercapacitor applications. These conduct-ing carbon materials provide a fast electron transfer rate during faradaic charge transfer reactions and hence enhance the capacitance. Additionally, these carbon nanomaterials provide a platform for the decoration of metal oxide nanoparticles to avoid their agglomeration, resulting in greater utilization of the nanoparticles.[15] Polymer–carbon nanocomposites provide a solution to the insulating nature of conducting polymers in doping states by using carbon nanomaterials as substrates to grow nanostructured polymers. The high cost of carbon nanotubes limits their commercial use on a large scale. Large-scale production of high quality graphene is still a challenge, which again limits the develop-ment of commercial graphene based supercapacitors.

Several research groups have developed PANI composites based on metal oxides or graphene for supercapacitors. For instance, Shi et al.[16] showed a large electrochemical capaci-tance of 210 F g^{-1} at a discharge rate of 0.3 A g^{-1} in composite films of chemically converted graphene (CCG) and polyaniline nanofibers (PANI-NFs) prepared by vacuum filtration of the mixed dispersions of both the components. Wang et al.[17] prepared one-dimensional and layered parallel folding of cobalt oxalate nanostructures and reported a maximum specific capacitance of 202.5 F g^{-1} at a current density of 1 A g^{-1} with a voltage window from 0 to 0.40 V. Baek et al.[18] have prepared a conducting polyaniline-grafted reduced graphene oxide (PANI-g-rGO) composite via acyl chemistry and reported a capacitance of 250 F g^{-1} with electrical conductivity as high as 8.66 S cm^{-1}. Lee et al.[19] reported specific capacitance as high as 637 F g^{-1} at a scan rate of 2 mV s^{-1} in a MnO_2 based composite prepared by coating amorphous MnO_2 onto crystal-line SnO_2 nanowires grown on a stainless steel substrate.

Huang et al.[20] have synthesized graphene/polyaniline (PANI) composite films using graphite oxide (GO) and aniline as the starting materials. They have reported a high specific capacitance value of 640 F g^{-1} with a retention life of 90% after 1000 charge–discharge cycles. Yu et al.[21] have prepared flexible graphene–PANI nanorod composite paper with uni-formly layered structures by in situ electropolymerization. The reported specific capacitance value of the flexible graphene–PANI paper composite was 763 F g^{-1} with good cycling stability. Wang et al.[22] have synthesized a flexible graphene/polyaniline hybrid material as a supercapacitor electrode by an in situ polymerization–reduction/dedoping–redoping process. They have reported a high specific capacitance value of 1126 F g^{-1} with a retention life of 84% after 1000 cycles. Fray et al.[23] have prepared highly porous nanorod-PANI–graphene compo-site films by in situ electrochemical polymerization onto an indium tin oxide (ITO) substrate in a reverse micelle electrolyte. The reported specific capacitance value was 878.57 F g^{-1} with a charge loading of 500 mC at a current density of 1 A g^{-1}.

In this study, we have demonstrated a simple and cost effective method for the preparation of a $CoCl_2$ doped PANI/GNP composite based low cost electrode material for super-capacitors which have very high specific capacitance values (≈ 635 F g^{-1}). Moreover, the composites reveal not only the behavior of a supercapacitor, but also high electrical con-ductivity (DC electrical conductivity ≈ 12.5 S cm^{-1}) at very low GNP content. The current–voltage measurements of the composite indicate semiconducting behavior of the composite that can be used in different electronics applications.

2. Experimental

2.1. Materials details

Aniline, potassium chloride and hydrated cobalt chloride ($CoCl_2 \cdot 6H_2O$) were procured from Merck, Germany. Cetyl trimethylammonium bromide (CTAB) and ammonium persul-fate (APS) [$(NH_4)_2S_2O_8$] were purchased from Loba Chemie Pvt. Ltd India. Multi-layer graphene nanoplates (GNPs, carbon purity: >99.5%, thickness: 8–10 nm, diameter: 5–25 μm, electrical conductivity: 10^7 S m^{-1}) were purchased from J. K. Impex, Mumbai, India.

2.2. Preparation of the PGC composites

Initially, 100 ml of 1.5 M HCl, GNP and CTAB were ultra-sonicated for 1 h, followed by vigorous stirring with a magnetic stirrer for 40 min at room temperature. Then, an aqueous solution of $CoCl_2 \cdot 6H_2O$ (prepared with de-ionized (DI) water) was added drop wise to this solution under constant stirring and stirring was continued for another 1 h at room temperature. Finally, 1 ml of aniline was added to this solution and stirred for 10 min. Then, ammonium persulfate (APS) solution prepared by dissolving 2 g of APS in 100 ml of 1.5 M HCl was added into the reaction media and stirring was continued. After 5 h, the solution became green and the $CoCl_2$ doped PANI/GNP composite (PGC) was precipitated. The
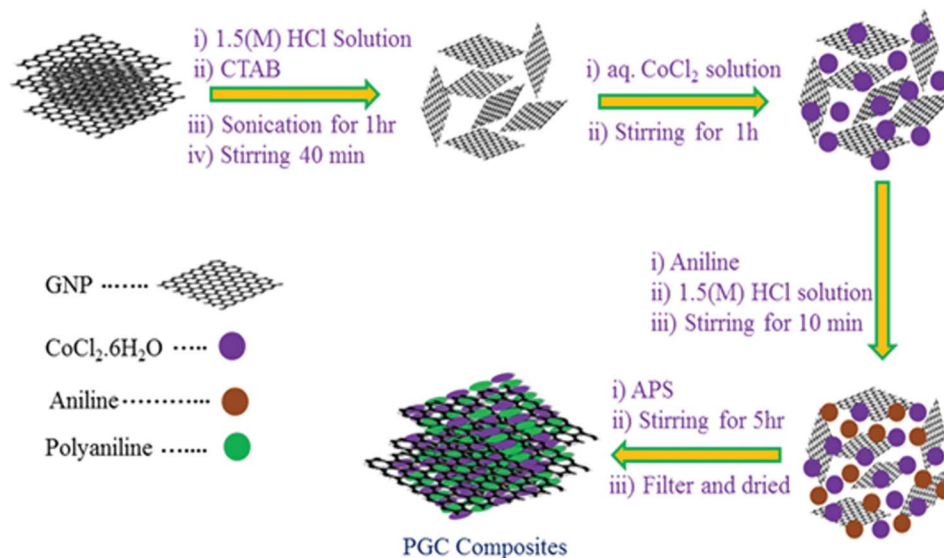
Fig. 1 Schematic representation for the preparation of PGC composites.

solution was filtered and washed with DI water several times to make the solution neutral and the residue was air dried for 24 h for further characterization. Here, a 1 : 3 molar ratio of aniline and $CoCl_2 \cdot 6H_2O$ was taken for preparation of the PGC composites with different GNP weight contents (denoted as PGC50, PGC100 and PGC200 for 50 mg, 100 mg and 200 mg GNP content). A schematic representation for the preparation of the PGC composites is shown in Fig. 1.

3. Characterization

3.1. Fourier transform infrared (FTIR) spectroscopy

FTIR of GNP and the PGC composites was studied using a NEXUS 870 FTIR (Thermo Nicolet) to investigate the structure of the GNP and PGC composites. For the FTIR spectrum, pelleted samples were prepared by mixing potassium bromide (KBr) and the material in the weight ratio 8 : 1.

3.2. Wide-angle X-ray diffraction (WAXD) analysis

The gallery height (*d*-spacing) of the GNP and PGC composites was measured by using a wide angle X-ray diffractometer, (WAXD, Rigaku, Ultima-III, Japan) with a nickel-filtered Cu-Kα line ($\lambda = 0.15404$ nm), operated at an accelerating voltage of 40 kV and 40 mA, at a scanning rate of $0.5°$ min^{-1}. The sample-to-detector distance was 400 mm. The gallery height of the ordered structure of the GNP and composite was calculated by using Bragg's law ($n\lambda = 2d\sin\theta$), where *d* is the distance between the planes (layers) in the ordered structure, λ is the wave length of the incident wave, θ is the angle between the incident wave and the scattering planes, and *n* is an integer.

3.3. Field emission scanning electron microscopy (FESEM)

The morphology of the PGC composites was studied using PGC pellets (prepared by pressing at room temperature) through FESEM (FESEM, Carl Zeiss-SUPRA™ 40), with an accelerating voltage of 5 kV. The samples were gold coated with a thin layer (approx. ∼5 nm) to avoid electrical charging. The gold coated composite sample was scanned in a vacuum on the order of 10^{-4} to 10^{-6} mm Hg.

3.4. High resolution transmission electron microscopy (HRTEM)

TEM analysis of the PGC composites was studied by HRTEM (HRTEM, JEM-2100, JEOL, Japan), operated at an accelerating voltage of 200 kV. A small amount of the PGC composite was dispersed in acetone through sonication. Then, the dispersed suspension of PGC composite was dropped on the copper (Cu) grid for HRTEM analysis.

3.5. Electrochemical characterization

Electrochemical analysis of as-synthesized PGC composites was performed by cyclic voltammetry (CV) with a CH instrument electrochemical analyzer. A three-electrode system was employed for all measurements where a PGC composite coated glassy carbon electrode, Pt wire and Ag/AgCl (KCl saturated; +197 mV) served as working, counter and reference electrode, respectively. For electrochemical characterization, we used 0.10 mg of PGC composite which was coated on a glassy carbon working electrode of 3 mm diameter. Cyclic voltammograms were recorded at different scan rates from 10 mV s^{-1} to 100 mV s^{-1} within potential windows from -1.0 to $+1.3$ V in 1 M KCl.

The electrochemical impedance spectroscopic (EIS) measurements were carried out in the frequency range 100 mHz–10 MHz. The specific capacitances (C_{sp}) of the PGC composites at different scan rates were calculated by using the following equation:

$$C_{sp} = (I_+ - I_-)/(v \times m) \tag{1}$$

where I_+ and I_- are the maximum currents in the positive and negative potential scans, respectively; v is the scan rate and m is the mass of the PGC composite.

The average energy density (E) of the PGC composite at different scan rates was evaluated by the following equation:

$$E = \frac{1}{2} C(\Delta V)^2 \qquad (2)$$

where ΔV represents the potential window.

3.6. I–V measurements

Current–voltage relationships of the PGC composites were measured with the pellet samples, using a Keithley 2400 source meter (lab view 18.1 protocol). The sample was placed on the probe station, from where two contacts were taken out. A positive voltage was applied from the top contact of the material, using the Keithley source meter.

3.7. Electrical conductivity

The DC electrical conductivity of the PGC composites was measured by a four probe method. The electrical conductivity of the samples was calculated with the help of the following equations:[24]

$$\text{Resistivity } (\rho, \ \Omega \text{ cm}) = \pi t / In2(V/I) \qquad (3)$$

$$\text{Conductivity } (\sigma, \ \text{S cm}^{-1}) = 1/\rho \qquad (4)$$

where V is the measured voltage, and I is the applied current. The thickness of the sample is represented by t. A minimum of five tests were performed for each specimen and the data was averaged.

The frequency dependent AC conductivity and dielectric permittivity of the PGC composites (disk type sample with thickness 0.3 cm and area 1.88×10^{-1} cm^2) were obtained using a computer controlled precision impedance analyzer (Agilent 4294A) by applying an alternating electric field (amplitude 1.000 V) across the sample cell in the frequency region of 40 Hz to 10 MHz. A parallel plate configuration was used for all the electrical measurements. A sample holder using a Pt probe was used for all the electrical measurements.

Parameters such as dielectric permittivity (ε') and dielectric loss tangent ($\tan\delta$) were obtained as a function of frequency. The AC conductivity (σ_{ac}) was calculated from the dielectric data using the relationship:

$$\sigma_{ac} \approx \omega\varepsilon_0\varepsilon'\tan\delta \qquad (5)$$

where ω is equal to $2\pi f$ (f is the frequency), and ε_0 is the vacuum permittivity. The dielectric permittivity (ε') was determined with the following equation:

$$\varepsilon' \approx C_p/C_0 \qquad (6)$$

where C_p is the observed capacitance of the sample (in parallel mode), and C_0 is the capacitance of the cell. The value of C_0 was calculated using the area (A) and thickness (d) of the sample, following the relationship:
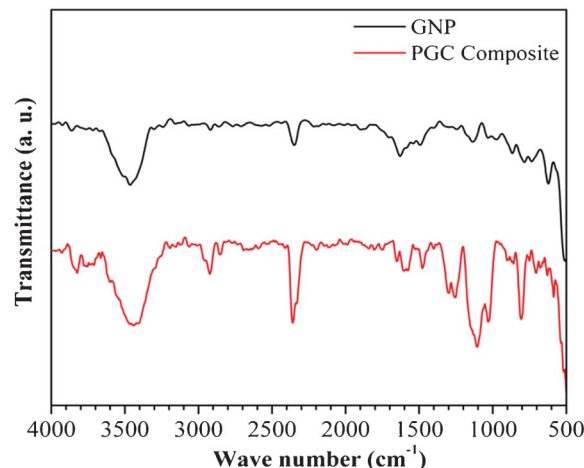

Fig. 2 Comparative FTIR analysis of GNP and PGC composite.

$$C_0 \approx (\varepsilon_0 \times A)/d \qquad (7)$$

4. Results and discussion

4.1. FTIR analysis

Fig. 2 shows the FTIR spectrum of pure GNP and PGC composites. The peaks for the PGC composites in the region of 2830–2971 cm^{-1}, 2986–3093 cm^{-1}, 1498 cm^{-1} and 718–1418 cm^{-1} indicate aliphatic C–H stretching, aromatic C–H stretching, aliphatic –CH$_2$ and different conformation sensitive vibration modes of PANI, respectively.[25] These characteristic peaks of PANI indicate the presence of PANI in the PGC composites. However, peaks for the GNP appear at 2348 cm^{-1}, 2918 cm^{-1} and 2858 cm^{-1}. These are the characteristic peaks of aromatic sp^2 C–H stretching vibrations. A broad peak appears at 3464 cm^{-1} for GNP which is attributed to the O–H stretching vibration. This is due to the absorption of moisture on the GNP surface. The spectral pattern of the GNP peaks has been slightly changed and the intensity is increased in the PGC composites. These changes of intensity in the PGC composites confirm the existence of the strong π–π interactions between electron rich PANI, CoCl$_2$ and GNP in the PGC composite which increase the capacitance and electrical conductivity value.

4.2. WAXD analysis

Fig. 3 shows the X-ray diffractograms of GNP powder and PGC composites. For GNP, an intense crystalline peak appears at a 2θ value of ~26.50°, which is the characteristic peak of hexagonal GNP with a d-spacing of 0.336 nm. In the case of the PGC composites, the characteristic peak for the GNP was observed at 2θ of ~26.46° along with other peaks. These different peaks have been observed due to the presence of cobalt salt in the PGC composite. Thus, WAXD analysis of the PGC composites confirmed the presence of inorganic cobalt salt in the composites.
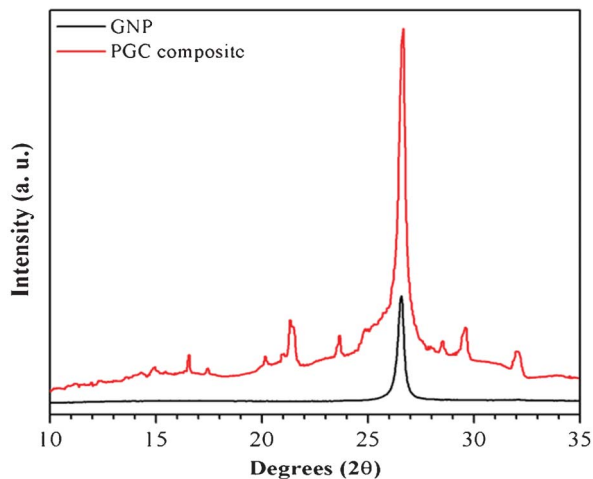
Fig. 3 Comparative WAXD analysis of GNP and PGC composites.

4.3. Morphology studies

The morphology of the GNP and PGC composites is shown in Fig. 4. Fig. 4a shows the HRTEM image of GNP without any chemical or surface modification. The, HRTEM image of the PGC composite is shown in Fig. 4b. As can be seen, $CoCl_2$ was successfully doped over the PANI and randomly interconnected throughout the PGC composite. This kind of interconnected network structure in the PGC composites generates electrical transport paths within the matrix polymer which may facilitate the electron transfer throughout the composites and enhances the capacitance value as well as electrical conductivity of the PGC composite. Fig. 4c shows the high magnification FESEM image of the PGC composites. This image also supports the successful doping of $CoCl_2$ on PANI over the GNP.

Fig. 5 shows the selected area electron diffraction (SAED) pattern images of pure GNP and PGC composite. Fig. 5a shows the SAED image of pure GNP powder. It shows the typical six fold symmetry and well defined crystalline nature of the GNP powder. However, this type of diffraction pattern disappears in the case of the PGC composite due to the presence of amorphous PANI, as shown in the SAED image in Fig. 5b.

4.4. Electrochemical analysis

4.4.1. Cyclic voltammetry (CV) analysis. The capacitive performances of the PGC50, PGC100 and PGC200 composites were measured by cyclic voltammetry (CV) in 1 M KCl solution to determine the specific capacitance (C_{sp}) and energy density of the devices in a three-electrode configuration with applied potential at different scan rates (10, 20, 50 and 100 mV s^{-1}), as shown in Fig. 6. The cathodic reduction and the anodic oxidation processes are responsible for the generation of negative and positive current regions in the cyclic voltammogram. The ideal rectangular shape of the cyclic voltammogram generally represents ideal capacitor behavior. The deviation of the ideality of the curve indicates pseudo-capacitive character of the PGC composites. This deviation from the ideal capacitor behavior arises due to the decrease in electrode and electrolyte
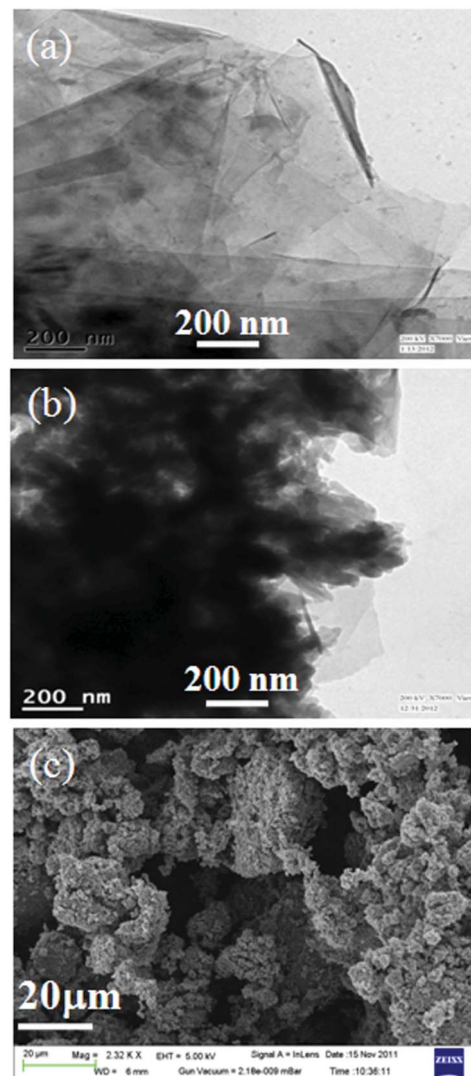

Fig. 4 HRTEM micrographs of (a) pure GNP and (b) PGC composite and (c) FESEM micrograph of PGC composite.

interaction.[26] Fig. 6a–6c show the cyclic voltammograms of PGC50, PGC100 and PGC200 composites at the different scan rates. The specific capacitance values of the PGC composites can be obtained with the help of the following equation:[27]
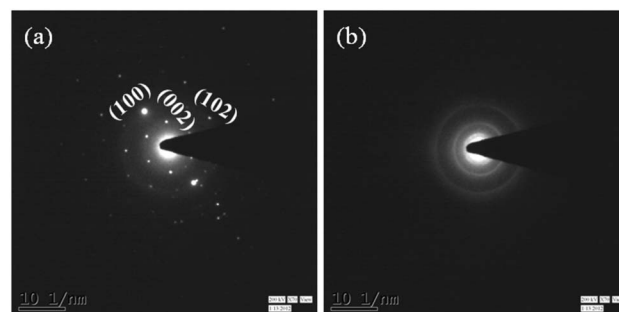

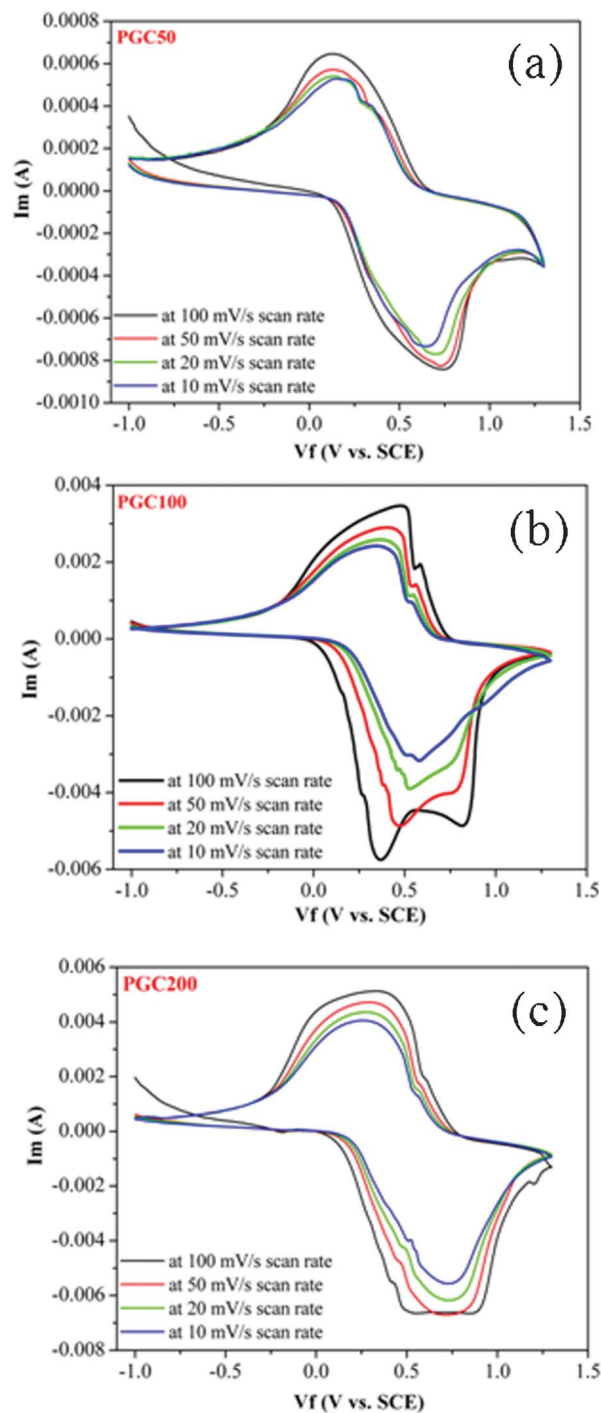**Fig. 5** SAED pattern of (a) GNP powder and (b) PGC composite.

Fig. 6 Cyclic voltammograms of the PGC composites at different scan rates.

$$C_{sp} = (I_+ - I_-)/(v \times m)$$

where, I_+ and I_- represent the maximum current in the positive and negative potential scan, respectively, v represents the scan rate and m represents the mass of the PGC composite.

On the basis of the cyclic voltammograms, PGC200 exhibited a higher specific capacitance (≈ 635 F g^{-1}) at a constant scan rate (10 mV s^{-1}) than those of PGC100 (500 F

g^{-1}) and PGC50 (80 F g^{-1}). Recent studies[28,29] have shown that the deposition of metal oxides or metal salts, such as RuO$_2$ nanoparticles and Ni(OH)$_2$ nanoplates, on reduced graphene oxide (RGO) sheets can improve the capacitive performance. It has also been reported that capacitive performance can be enhanced by preparing thin films consisting of PANI fibers and RGO sheets.[30] These improvements of the high capacitive performances of the composites are due to the contributions of the high electrical conductivity of RGO and the pseudo-capacitance of the metal oxides/metal salts or conducting polymer.

In the present study, the noteworthy enhancement in the specific capacitance of the PGC200 composite can also be attributed to the contributions of all components, such as PANI, GNP and hydrated CoCl$_2$. The effective charge transfer in the electrode plays a key role in improving the specific capacitance and rate capability. Effective anchoring of the hydrated CoCl$_2$/PANI on the GNP sheets facilitates easy and fast ion transport in the electrode material, and ultimately improves the electrical capacitance. In the PGC composites, CoCl$_2$ doped PANI supported on GNP sheets increases the intimate interaction of both the components that enhance the charge transfer between the components with high electrical conductivity. This huge improvement in the capacitance value in the PGC composites may be attributed to the additional faradaic charge transfer involved at the electrode–electrolyte interface due to the presence of metal salts.

The specific capacitance of the PGC composites as a function of scan rate is shown in Fig. 7. In addition, the difference in the specific capacitance value for all the composites (PGC50, PGC100, and PGC200) can be observed from the figure at different scan rates. As observed, the specific capacitance value of the PGC composites strongly depends on the area under the cyclic voltammogram, consistent with the previous reports.[2]

Cyclic voltammetry of the PGC composites was performed at different scan rates of 10, 20, 50, and 100 mV s^{-1} for each sample. As can be seen, the specific capacitance of the composites strongly depends on the scan rate and it gradually
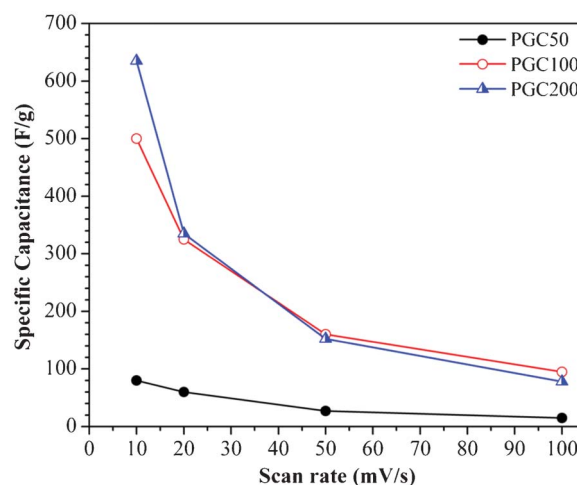

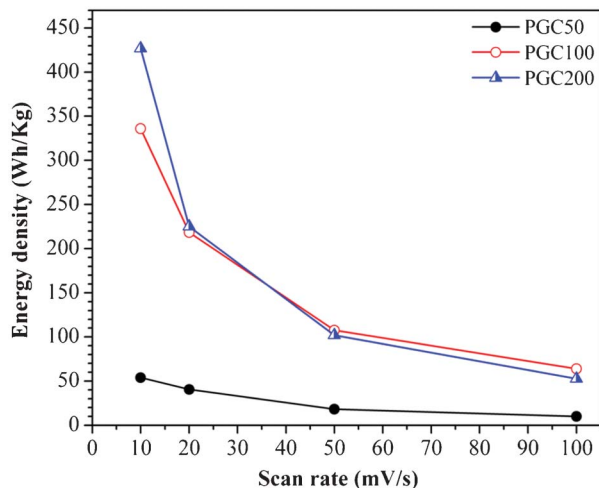Fig. 7 Plot of specific capacitance vs. scan rate for PGC composites.

Fig. 8 Plot of energy density *vs.* scan rate for PGC composites.

decreases for all the PGC composites at a higher scan rate, as shown in Fig. 7. At a high scan rate, high diffusion resistance and large electrochemical polarization affects the electrode material which reduces the capacitive behavior of the composites and hence reduces the specific capacitance value.[31] This suggests a high degree of sustainability of the capacitance of the composites even at a higher scan rate. The doping of $CoCl_2$ on PANI increases the π–π stacking interaction between GNP, $CoCl_2$ and PANI chains, which may facilitate electron transfer and has a synergistic effect on the electrochemical properties of the hybrid composites.[32] This may be attributed by decreasing internal resistance compared with PANI electrode.

Fig. 8 shows the variation of energy density of the PGC composites with different scan rates. From the figure, it is clearly seen that the energy density of the PGC composites decreases with increasing scan rate, similar to the specific capacitance value. PGC200 composites show the highest energy density value (≈ 427 W h kg^{-1}) at a 10 mV s^{-1} scan

rate. This high energy density is attributed to the extended conductive network structure of the GNP and strong interlayer π–π interaction between the GNP and electron rich PANI matrix. Thus, it reduces the internal resistance and increases the electrolyte ion transport rate during electrochemical performance.

4.4.2. Constant current charging–discharging (CCD) analysis. Fig. 9 shows the constant current charging–discharging (CCD) analysis for the PGC100 and PGC200 composites. The CCD analysis for the composites was carried out at a constant current density of 10 mA g^{-1}. From the figure, *IR* drops are observed in the case of PGC100 composite, however, a triangular shaped symmetric charge–discharge curve is observed in the case of the PGC200 composite which indicates ideal capacitive nature of the composite. The specific capacitance (C_{sp}) of the composite was estimated from the charge–discharge curve with the help of the following equation:[33]

$$C_{sp} = \frac{(I \times \Delta t)}{(\Delta V \times m)} \tag{8}$$

where *I* is applied current, ΔV is the voltage, Δt is the average time in seconds and *m* signifies the mass of the PGC composite. The obtained specific capacitance values for the PGC100 and PGC200 composites were 512 F g^{-1} and 647 F g^{-1}, respectively.

4.4.3. Cycle-life stability test. The long-term cycle stability of the PGC composites was calculated by repeating the cyclic voltammetry (CV) in 1 M KCl electrolyte at a scan rate of 10 mV s^{-1} for 500 cycles.

Fig. 10 shows the specific capacitance as a function of cycle number for the PGC50, PGC100 and PGC200 composites. As can be seen, the PGC200 composite retains 85% specific capacitance after 500 cycles. The PGC100 and PGC50 composites retain 81% and 60% specific capacitance after the same number of cycles. However, the specific capacitance of the composites decreases upon increasing the cycle number, as shown in Fig. 10. The intermolecular and π–π interaction between the GNP, PANI and $CoCl_2$ restricts the
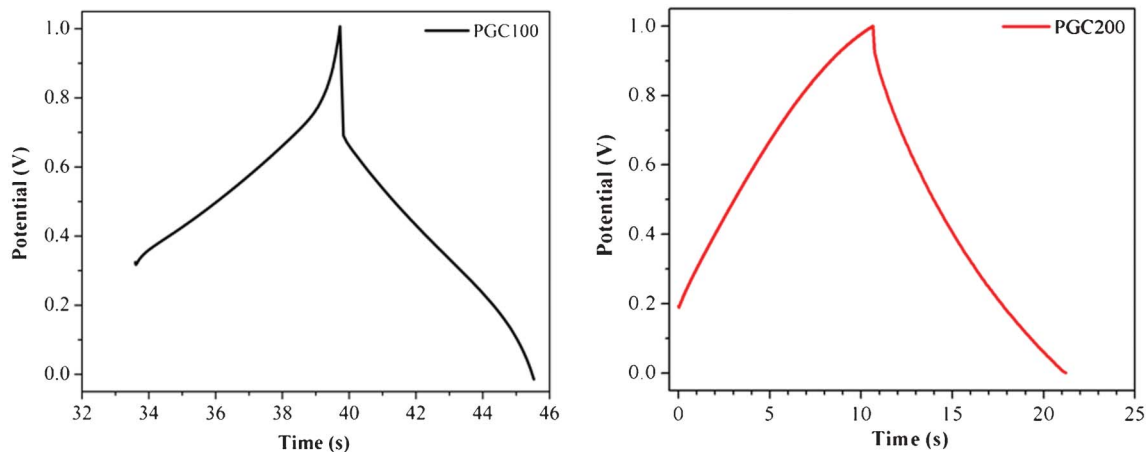

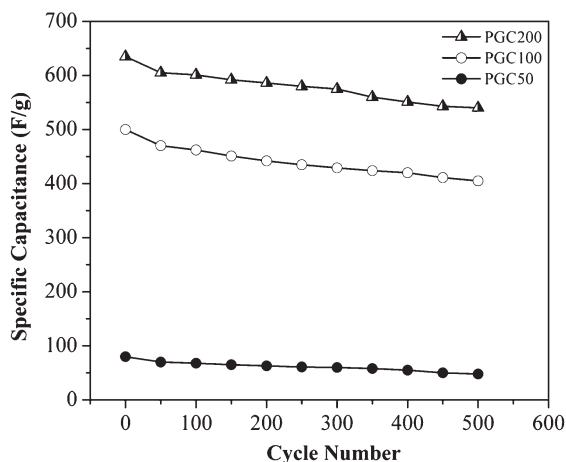**Fig. 9** Cyclic charge–discharge curves of PGC composites.

Fig. 10 Specific capacitance *vs.* cycle number of PGC composites in 1 M KCl solution.

change of the regular network structure and increases the cycle stability of the PGC composites. The extended network structure in the PGC composites is also the reason for the increasing cycle stability.

4.4.4. Electrochemical impedance spectroscopic (EIS) analysis. Fig. 11 shows the Nyquist plot of impedance and a suitable circuit for the PGC composites. The Nyquist plot of impedance

gives information about the electrochemical impedance behavior of the composites. As observed in Fig. 11a–11c, the real component (Z') represents the ohmic properties. On the other hand, the imaginary component (Z'') stands for the capacitive properties.[34] This study has been carried out in the frequency region 100 mHz–10 MHz. For an ideal super-capacitor, the Nyquist plot shows three frequency dependent regions.[35] In the high frequency region, it shows behavior like a pure resistor. However, pure capacitive behavior is observed in the low frequency region where the imaginary part sharply increases and a vertical line is observed. In the case of the medium frequency domain, the influence of the electrode porosity can be observed. The electrolyte penetrates deeper and deeper into the porous structure of the electrode when the frequency decreases from the very high frequency and results in more and more electrode surface being available for ion adsorption. This medium frequency range is known as a Warburg curve. However, it is impossible to get an ideal supercapacitor in the real world. Solution resistance (R_s) of the composites can be obtained from the intercepts at the highest frequency of the curves on the real axis.

The smaller semicircle at the higher frequency region in the Nyquist plots indicates the charge transfer resistance (R_{ct}). Warburg resistance (W) of the composites is observed in the intermediate frequency region. In general, the non-ideal behavior of the capacitors is expressed by the constant phase element (CPE) and denoted by an 'n' value.[36,37] The Nyquist
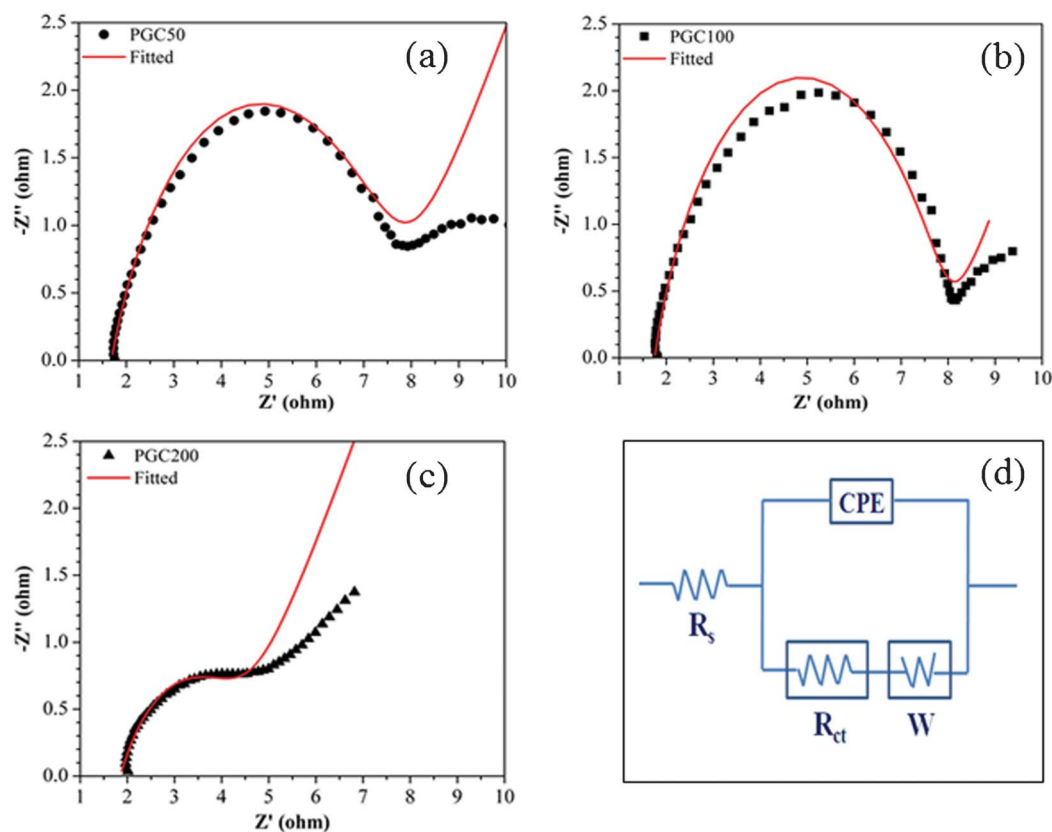

Fig. 11 Nyquist plots and equivalent electrical circuit used in EIS fitting data for the PGC composites.

plots were analyzed by fitting the experimental impedance spectra to an equivalent electrical circuit. Thus, a suitable circuit for the PGC composites has been schematically demonstrated in Fig. 11d. From the figure, it is seen that semicircle is obtained at high frequency and a straight line is observed at the low frequency regions. The R_s value for the PGC composite was found to be 1.685 Ω. The π–π interaction between GNP, $CoCl_2$ and PANI is the probable reason behind the low R_s value which allows efficient electrolyte accessibility to the electrode surface by shortening the ion diffusion pathway. The high electrical conductivity and enhanced capacitive properties of the PGC composite are well supported by the low R_s value. The vertical line at low frequency in the plots is an indication of good capacitive behavior and low diffusion resistance of the electrode material, which is also attributed to the low Warburg resistance. However, the quality of the electrode material depends on the 'n' value which is obtained from the CPE. For ideal capacitors, the n value will be equal to 1 and for insulators, it will be zero. In this study, the n value of all PGC composites lies between 0.7 and 0.825 (>0.5). This result leads us to assume that the PGC composites behave like a moderate capacitor.

4.5. Comparative study

Li et al.[38] reported a capacitance value of 1130 F g^{-1} at a 5 mV s^{-1} scan rate for the composite based on graphene nanosheets and PANI nanofibers. The composite was prepared by in situ polymerization in 1 M H_2SO_4 solution having a long cycle life with 87% specific capacitance retention after 1000 charge–discharge processes. Wang et al.[39] have shown high specific capacitance of 1126 F g^{-1} for flexible graphene/PANI hybrid materials which were synthesized by an in situ polymerization–reduction/dedoping–redoping process. Yan et al.[40] have synthesized a graphene nanosheet/PANI composite by an in situ polymerization method and reported a specific capacitance value of 1046 F g^{-1} at a 1 mV s^{-1} scan rate with an energy density of 39 W h kg^{-1}. Zhang et al.[41] have prepared a PANI-doped graphene composite and obtained a specific capacitance of 480 F g^{-1} at a current density of 0.1 A g^{-1}. Liu et al.[42] reported a specific capacitance of 301 F g^{-1} for a flexible graphene sheet/PANI nanofiber composite. Wang et al.[43] have synthesized a flexible graphene/PANI composite by an in situ electro-polymerization method and achieved a gravimetric capacitance of 233 F g^{-1} and a volumetric capacitance of 135 F cm^{-3}. Wu et al.[44] prepared graphene and PANI nanofiber composite films that exhibited electrochemical capacitance of 210 F g^{-1} at a discharge rate of 0.3 A g^{-1}. Sahoo et al.[45] reported a specific capacitance of 466 F g^{-1} at a 10 mV s^{-1} scan rate in a nanocomposite based on graphene and polypyrrole (PPy) nanofibers using sodium alginate.

4.6. Current (I)–voltage (V) relationship

The I–V relationships for the PGC composites were measured at room temperature (302 K) within the potential window of −5 V to +5 V and are shown in Fig. 12. A nonlinear increase in current (A) was observed with the applied voltage (V). This indicates a non ohmic behavior of the PGC composites. This nonlinear nature of the PGC composites indicates their
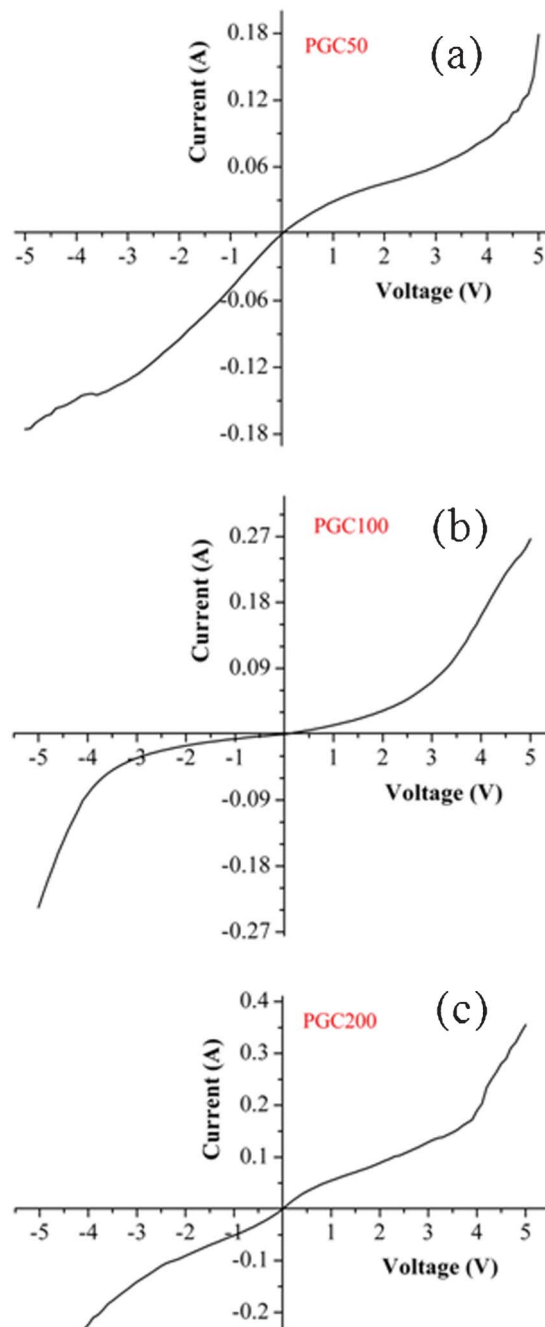

Fig. 12 I–V plots of PGC composites.

semiconducting behavior.[40] Thus, this material can be used in different electronic devices. Bora et al. studied the I–V characteristics of graphene oxide/PPy composites and reported similar types of results.[46]

4.7. Electrical properties

4.7.1. DC conductivity. Fig. 13 shows the room temperature measurements of DC electrical conductivity (σ_{DC}) of the PGC composites with different GNP contents.

It is observed that the σ_{DC} value of the PGC composites increased with increasing GNP content in the composite.
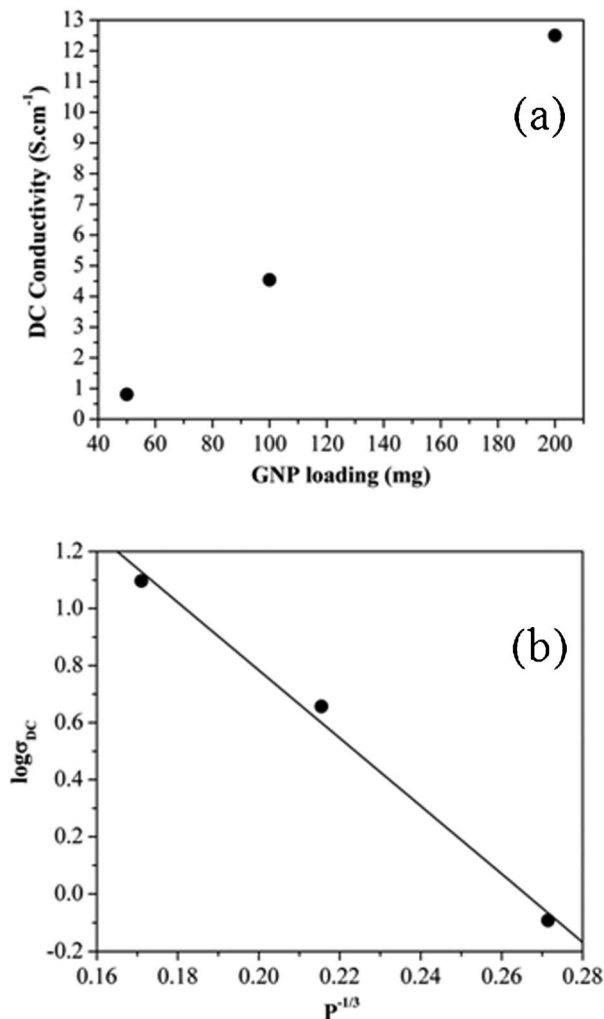
Fig. 13 Plot of (a) DC conductivity *vs.* GNP loading, and (b) log σ_{DC} *vs.* $p^{-1/3}$ for the PGC composites.

Finally, the PGC50 composite exhibited an electrical conductivity of ≈0.81 S cm⁻¹ after optimization of the different PGC composites. This very high electrical conductivity of the composite can be explained considering the formation of a continuous conductive interconnected network structure of the GNP–GNP and GNP–PANI throughout the polymer phase even at exceptionally low GNP loading. Thus, net σ_{DC} of the PGC composites was greatly increased upon increasing the amount of GNP in the composites. The σ_{DC} of the PGC100 composites was ≈4.54 S cm⁻¹ and that of PGC200 was ≈12.5 S cm⁻¹, which is a very high conductive value, as shown in Fig. 13a. This high electrical conductivity of the PGC composite is well supported by capacitance and EIS behavior of the composite.

According to percolation theory, an infinite cluster of interconnected conductive network paths of nanofillers has been formed at the critical concentration throughout the matrix phase, which is the reason behind the insulator–conductor transition. Two particles are supposed to be connected when they are in physical contact. Electrical conductivity in the composites is higher than that in the insulating or less conductive polymer before the formation of a continuous network of paths of fillers or particles. This is expected for the presence of an inter-particle conduction mechanism. Grossiord *et al.* have reported[47] that the electrical conductivity properties in polymer nanocomposites might arise due to the effect of a tunneling mechanism. Ryvkina *et al.*[48] explained that the conduction of polymer/carbon black (CB) composites was dominated by an electron tunneling mechanism on the basis of a theoretical model, with the following relationship:

$$\sigma_{DC} \propto \exp(-Ad) \quad (9)$$

where A stands for the tunnel parameter and d represents the tunnel distance. Recently, the presence of a tunneling conduction mechanism for various composite systems has been well explained in the literature. In a tunneling conduction mechanism, the charge carriers move through the polymer composites across the insulating gaps between fillers. In polymer composites, electrical conduction is generated by tunneling of charge carriers among nanofillers. These charge carriers can be generated by physical contact between the nanofillers or even if they are separated by insulating gaps in their pathways. The existence of tunneling conduction which contributes to the current through the composites may be one of the reasons for the variation of the conductive properties.[49] The properties of the energy barrier change with the host polymer and the fabrication process. The current in a tunnel junction strongly depends on the barrier width and exponentially decreases with it. If fillers are randomly distributed, then the mean average distance (d) among the fillers would be equal to that of the barrier width. This distance is assumed, in the first approximation, to be directly proportional to the nanofillers' concentration by weight, $p^{-1/3}$.[50]

$$d \propto p^{-1/3} \quad (10)$$

Thus, the tunneling assisted conductivity (log σ_{DC}) derived from eqn (9) and (10) is directly proportional to $p^{-1/3}$ and can be expressed by the following equation:

$$\log(\sigma_{DC}) \propto p^{-1/3} \quad (11)$$

From Fig. 13b, it is clearly shown that log σ_{DC} for the PGC composites varies linearly with $p^{-1/3}$. This linear relationship indicates that the tunneling mechanism is the reason for the development of electrical conductivity in the composites. Therefore, tunneling of the electrons occurs between the neighboring nanofillers. Normally, the electrons in a polymer phase cannot move from one electrode to another as the energy barrier is very high in the insulating or less conductive polymer matrix. However, the energy barrier gap decreases when a voltage is applied from the source between the two electrodes. This is the driving force for the movement of electrons to overcome the energy barrier by tunneling conduction. Thus, the electrons in the composites are tunneling from one electrode to the adjacent electrode when
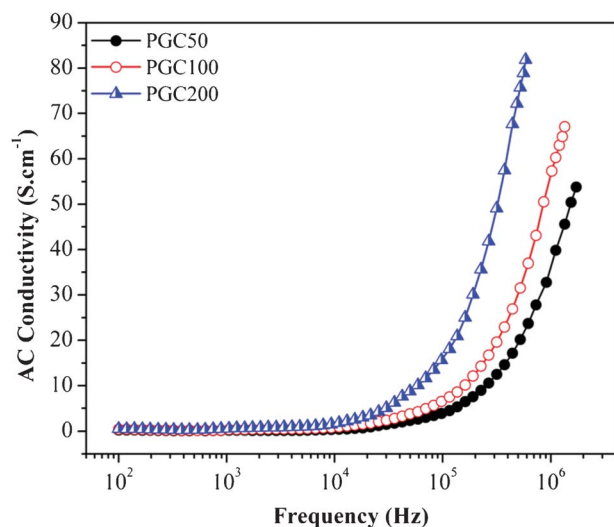
Fig. 14 AC conductivity of the PGC composites *vs.* frequency at different GNP contents.

the energy barrier is sufficiently low and form a continuous interconnected GNP–GNP network path throughout the matrix. So, it reduces the contact resistance and increases the electrical conductivity of the composites.

4.7.2. AC conductivity. The frequency (f) dependent AC electrical conductivity of the PGC composites is shown in Fig. 14. This measurement was carried out in the frequency region $\sim 10^1$ Hz to $\sim 10^7$ Hz at room temperature.

It can be clearly observed from Fig. 14 that the AC electrical conductivity of the PGC composites increased with increasing frequency and also with increasing GNP content in the composites. The AC electrical conductivity of the PGC composites was frequency independent up to a certain frequency region from ~ 50 to $\sim 10^4$ Hz and then suddenly increased in the frequency region $\sim 10^4$ to $\sim 10^7$ Hz, as shown in Fig. 14. The results in Fig. 14 show that the AC electrical conductivity remained almost constant up to a certain frequency, known as the critical frequency (f_c). However, the electrical conductivity strongly varies with the frequency when the frequency (f) is greater than f_c and it can be described by the following relationship, considering a first approximation value:

$$\sigma_{AC} \propto f^s \tag{12}$$

where s represents an exponent.

Many researchers[51,52] have found that the generation of AC electrical conductivity in composites is due to electron hopping and electron tunneling between nanofillers. Thus, AC electrical conductivity in the composites is directly proportional to the electron hopping and also depends on the electron tunneling mechanism. Upon increasing the GNP content in the composites, the development of the interconnected conductive network structure of GNP–GNP increased throughout the PGC composites. This will have helped to increase the rate of electron hopping or the electron tunneling pathway above a percolation threshold in the composites

which significantly increased the electrical conductivity of the composites.

The AC electrical conductivity (σ_{AC}) of any dielectric material below f_c (in the low frequency range) is the summation of two components and can be expressed in terms of the DC electrical conductivity (σ_{DC}), angular frequency (ω, which is equal to $2\pi f$) and dielectric loss factor (ε'') by the following equation:

$$\sigma_{AC} = \sigma_{DC} + \omega\varepsilon'' \tag{13}$$

The first component of the equation is σ_{DC} which arises due to the ionic or electronic conductivity and the value of the second component ($\omega\varepsilon''$) in the relationship strongly depends on the extent of polarization of dipoles (permanent and induced) and accumulated interfacial charges, known as the Maxwell–Wagner–Sillars (MWS) effect. The effect of interfacial polarization becomes more significant in the low frequency region (below f_c) as the dipoles/induced dipoles get enough time to orient themselves with the direction of applied electric field (relaxation phenomenon). Thus, the value of σ_{AC} for a conductive system truly represents σ_{DC} in the low frequency region. The frequency independence of the electrical conductivity for different disordered materials below f_c has already been reported.[51,53]

In the high frequency region (above f_c), the polarization effect becomes unimportant as the dipoles get insufficient relaxation time to orient themselves in the direction of the applied electric field. The applied AC electric field (periodic alternation) above f_c results in the radical reduction of space charge accumulation and dispersion of dipoles in the applied field direction that reduces the extent of polarization. Thus, the value of σ_{AC} strongly depends on the excitation of the charge particles and flow of electrons through the continuous conductive network in the matrix phase. Furthermore, it can be assumed that above f_c, the hopping of excited electrons through the inter particle gap (thin polymer layer) becomes easier, adding to the conductivity that already exists at low frequency in the composites. The frequency dependent dielectric permittivity (ε') of the PGC composite was measured in the frequency region 50 Hz–10^7 Hz at room temperature and is available in the ESI.† This PGC composite can also be used as a dielectric material.

5. Conclusion

In summary, polymeric supercapacitor material based on $CoCl_2$ doped PANI/GNP composites (PGC) has successfully been prepared by a simple and industrially feasible method. The morphology, capacitive behavior and electrical properties of the PGC composites were thoroughly studied. A nonlinear increase in current with the applied voltage indicates a non ohmic behavior, suggesting the semiconducting nature of the PGC composites. A gradual decrease in dielectric permittivity of the PGC composites with an increase in frequency in the lower frequency region represents the characteristics of a dielectric material in the composites. The specific capacitance value of ≈ 635 F g^{-1} at 10 mV s^{-1} was obtained in the PGC

composites along with high electrical conductivity (≈ 12.5 S cm^{-1}). The π–π stacking interaction between the phenyl rings of PANI and GNP in the PGC composites increases the specific capacitance value, as well as the electrical conductivity. This high capacitance value suggests that PGC composites can be considered as highly promising materials for supercapacitor applications.

Acknowledgements

References

1 J. R. Miller and P. Simon, *Science*, 2008, **321**, 651.
2 B. Z. Jang, C. Liu, D. Neff, Z. Yu, M. C. Wang, W. Xiong and A. Zhamu, *Nano Lett.*, 2011, **11**, 3785.
3 C.-G. Karina, L.-C. Monica, C.-P. Nieves and G.-R. Pedro, *Adv. Funct. Mater.*, 2005, **15**, 1125.
4 Y. Wang, Z. Shi, Y. Huang, Y. Ma, C. Wang, M. Chen and Y. Chen, *J. Phys. Chem. C*, 2009, **113**, 13103.
5 T. Y. Kim, H. W. Lee, M. Stoller, D. R. Dreyer, C. W. Bielawski, R. S. Ruoff and K. S. Suh, *ACS Nano*, 2010, **5**, 436.
6 N. Liu, L. Yin, C. Wang, L. Zhang, N. Lun, C. Wang and Y. Qi, *J. Phys. Chem. C*, 2010, **114**, 22012.
7 P. Simon and Y. Gogotsi, *Nat. Mater.*, 2008, **7**, 845.
8 M. Winter and R. Brodd, *Chem. Rev.*, 2005, **105**, 1021.
9 L. L. Zhang and X. S. Zhao, *Chem. Soc. Rev.*, 2009, **38**, 2520.
10 A. S. Arico, P. Bruce, B. Scrosati, J. M. Tarascon and W. Van Schalkwijk, *Nat. Mater.*, 2005, **4**, 366.
11 P.-C. Chen, G. Shen, Y. Shi, H. Chen and C. Zhou, *ACS Nano*, 2010, **4**, 4403.
12 J. Zhang, J. Ma, L. L. Zhang, P. Guo, J. Jiang and X. S. Zhao, *J. Phys. Chem. C*, 2010, **114**, 13608.
13 Y. Li, X. Zhao, Q. Xu, Q. Zhang and D. Chen, *Langmuir*, 2011, **27**, 6458.
14 D. Chen, H. Feng and J. Li, *Chem. Rev.*, 2012, **112**, 6027.
15 J. W. Lee, A. S. Hall, J.-D. Kim and T. E. Mallouk, *Chem. Mater.*, 2012, **24**, 1158.
16 Q. Wu, Y. Xu, Z. Yao, A. Liu and G. Shi, *ACS Nano*, 2010, **4**, 1963.
17 D. Wang, Q. Wang and T. Wang, *Inorg. Chem.*, 2011, **50**, 6482.
18 N. A. Kumar, H.-J. Choi, Y. R. Shin, D. W. Chang, L. Dai and J.-B. Baek, *ACS Nano*, 2012, **6**, 1715.
19 J. Yan, E. Khoo, A. Sumboja and P. S. Lee, *ACS Nano*, 2010, **4**, 4247.
20 X.-M. Feng, R.-M. Li, Y.-W. Ma, R.-F. Chen, N.-E. Shi, Q.-L. Fan and W. Huang, *Adv. Funct. Mater.*, 2011, **21**, 2989.
21 H.-P. Cong, X.-C. Ren, P. Wang and S.-H. Yu, *Energy Environ. Sci.*, 2013, **6**, 1185.
22 H. Wang, Q. Hao, X. Yang, L. Lu and X. Wang, *Nanoscale*, 2010, **2**, 2164.
23 L. Hu, J. Tu, S. Jiao, J. Hou, H. Zhua and D. J. Fray, *Phys. Chem. Chem. Phys.*, 2012, **14**, 15652.
24 S. Bose, T. Kuila, M. E. Uddin, N. H. Kim, A. K. T. Lau and J. H. Lee, *Polymer*, 2010, **51**, 5921.
25 A. Y. Arasi, J. J. L. Jeyakumari, B. Sundaresan, V. Dhanalakshmi and R. Anbarasan, *Spectrochim. Acta, Part A*, 2009, **74**, 1229.
26 S. K. Meher, P. Justin and G. R. Rao, *ACS Appl. Mater. Interfaces*, 2011, **3**, 2063.
27 S. Sahoo, G. Karthikeyan, G. C. Nayak and C. K. Das, *Synth. Met.*, 2011, **161**, 1713.
28 D. Zhao, X. Guo, Y. Gao and F. Gao, *ACS Appl. Mater. Interfaces*, 2012, **4**, 5583.
29 Z. Sun and X. Lu, *Ind. Eng. Chem. Res.*, 2012, **51**, 9973.
30 Z. Gao, W. Yang, J. Wang, B. Wang, Z. Li, Q. Liu, M. Zhang and L. Liu, *Energy Fuels*, 2013, **27**, 568.
31 Y. Zhang, G.-Y. Li, Y. Lv, L.-Z. Wang, A.-Q. Zhang and Y.-H. Song, *et al.*, *Int. J. Hydrogen Energy*, 2011, **36**, 11760.
32 S. Biswas and L. T. Drzal, *Chem. Mater.*, 2010, **22**, 5667.
33 Y. Wang, Z. Shi, Y. Huang, Y. Ma, C. Wang, M. Chen and Y. Chen, *J. Phys. Chem. C*, 2009, **113**, 13103.
34 W. Chen, R. B. Rakhi, L. Hu, X. Xie, Y. Cui and H. N. Alshareef, *Nano Lett.*, 2011, **11**, 5165.
35 Q. Cheng, J. Tang, J. Ma, H. Zhang, N. Shinya and L.-C. Qin, *J. Phys. Chem. C*, 2011, **115**, 23584.
36 J. Liu, J. An, Y. Ma, M. Li and R. Ma, *J. Electrochem. Soc.*, 2012, **159**, A828.
37 X. Feng, R. Li, Z. Yan, X. Liu, R. Chen and Y. Ma, *et al.*, *IEEE T Nanotechnol.*, 2012, **99**, 1.
38 J. Li, H. Xie, Y. Li, J. Liu and Z. Li, *J. Power Sources*, 2011, **196**, 10775.
39 H. Wang, Q. Hao, X. Yang, L. Lu and X. Wang, *Nanoscale*, 2010, **2**, 2164.
40 J. Yan, T. Wei, B. Shao, Z. Fan, W. Qian and M. Zhang, *et al.*, *Carbon*, 2010, **48**, 487.
41 D. Zhang, X. Zhang, Y. Chen, P. Yu, C. Wang and Y. Ma, *J. Power Sources*, 2011, **196**, 5990.
42 S. Liu, X. Liu, Z. Li, S. Yang and J. Wang, *New J. Chem.*, 2011, **35**, 369.
43 D.-W. Wang, F. Li, J. Zhao, W. Ren, Z.-G. Chen and J. Tan, *et al.*, *ACS Nano*, 2009, **3**, 1745.
44 Q. Wu, Y. Xu, Z. Yao, A. Liu and G. Shi, *ACS Nano*, 2010, **4**, 1963.
45 S. Sahoo, S. Dhibar, G. Hatui, P. Bhattacharya and C. K. Das, *Polymer*, 2013, **54**, 1033.
46 C. Bora and S. K. Dolui, *Polymer*, 2012, **53**, 923.
47 N. Grossiord, J. Loos, L. van Laake, M. Maugey, C. Zakri, C. E. Koning and A. J. Hart, *Adv. Funct. Mater.*, 2008, **18**, 3226.
48 N. Ryvkina, I. Tchmutin, J. Vilcakova, M. Peliskova and P. Saha, *Synth. Met.*, 2005, **148**, 141.
49 Y. Gefen, A. Aharony and S. Alexander, *Phys. Rev. Lett.*, 1983, **50**, 77.
50 A. Bello, E. Laredo, J. R. Marval, M. Grimau, M. L. Arnal and A. J. Muller, *Macromolecules*, 2011, **44**, 2819.
51 D. Wu, Y. Zhang, M. Zhang and W. Yu, *Biomacromolecules*, 2009, **10**, 417.
52 J. C. Dyre, *J. Appl. Phys.*, 1988, **64**, 2456.
53 J. C. Dyre and T. B. Schroder, *Rev. Mod. Phys.*, 2000, **72**, 873.